Preprint Title	The impact of tris(pentafluorophenyl)borane hole transport layer doping on interfacial charge extraction and recombination
Authors	Konstantinos Bidinakis and Stefan A. L. Weber
Publication Date	30 Juli 2024
Article Type	Full Research Paper
Supporting Information File 1	Supporting_Bidinakis v2.docx; 3.1 MB
ORCID® iDs	Konstantinos Bidinakis - https://orcid.org/0009-0007-5131-3399; Stefan A. L. Weber - https://orcid.org/0000-0003-3052-326X

The impact of tris(pentafluorophenyl)borane hole transport layer doping on interfacial charge extraction and recombination

Konstantinos Bidinakis[1] and Stefan A.L. Weber*[1,2]

Address: [1]Max Planck Institute for Polymer Research, Ackermannweg 10, 55128 Mainz, Germany

[2]Institute for Photovoltaics, University of Stuttgart, Pfaffenwaldring 47, 70569 Stuttgart, Germany

Email: Stefan A.L. Weber - stefan.weber@ipv.uni-stuttgart.de

* Corresponding author

Abstract

Selective charge transport layers have a strong influence on the overall efficiency and stability in perovskite solar cell devices. Specifically, the charge extraction and recombination occurring at the perovskite's interfaces with these materials can be a limiting factor for performance. A lot of effort has been put into improving the conductivity of selective contacts, as well as the junction quality and energetic alignment with the absorber. On the hole extracting side, organic semiconductors have been extensively used due to their flexibility and favorable properties. Two such compatible materials that have yielded high performing devices are the small molecule 2,2',7,7'-Tetrakis[N,N-di(4-methoxyphenyl)amino]-9,9'-spirobifluorene (spiro-OMeTAD) and the polymer Poly[bis(4-phenyl)(2,4,6-trimethylphenyl)amine (PTAA). In this work, we investigate the impact of hole transport layer doping on the performance

and potential distribution in solar cells based on these materials. To do so on operating solar cells, we created samples with exposed cross-sections and examined their potential profile distributions with Kelvin probe force microscopy (KPFM), implementing our comprehensive measurement protocol. Using the Lewis acid tris(pentafluorophenyl)borane (BCF) enhanced the hole extracting material/perovskite junction quality in spiro-OMeTAD and in PTAA based devices. Measurements under illumination show that the improvement is caused by a reduced recombination rate at the perovskite/hole transporter interface.

Keywords

perovskite solar cells; kelvin probe force microscopy; cross-section

Introduction

Perovskite solar cells (PSCs) are a promising class of photovoltaic material that exhibit high power conversion efficiencies and rely on a low cost solution-processed fabrication method [1-4]. At the core of their success lies the perovskite absorber material, which exhibits impressive bulk properties, such as long carrier lifetimes and low recombination rates [5-8]. However, the granular nature of perovskites and the layered structure of their solar cells, introduce complications such as grain boundaries and interfacial defect states that hinder performance. Specifically, since the interaction of adjacent layers at the solar cell's interfaces is an important limiting factor for its operation, there is a need for dedicated studies regarding interfacial behavior. Kelvin probe force microscopy (KPFM) provides us with an important tool for conducting such studies, by allowing us to measure the perovskite's surface potential by monitoring the electrostatic force between each point of the surface and a conductive probe (See

Supporting Information File 1). This measurement can provide insights about charge generation and transport within the absorber material, as well as extraction to the relevant interfaces [9-12].

The details of interfacial electronic carrier extraction at the junctions of the perovskite with the electron and hole transport layers (ETL, HTL) define the ability of a solar cell to give out electrical current optimally. Particularly, the relative capability of the two interfaces to extract and block charges properly is critical, because issues such as energetic misalignment, trap states and interfacial recombination may lead to an uneven extraction and therefore a charge accumulation within the perovskite. Initial studies suggested that this asymmetrical charge carrier behavior indicates an unfavorable hole extraction and a promoted electron extraction [9,13,14], but the migration and interaction of mobile ions (such as I^- ions interacting with spiro-OMeTAD [15,16] and Li^+ ions interacting with TiO_2 [17,18]) has also been proposed to explain the asymmetrical distribution of charges within the perovskite [19,20].

Many research endeavors involve the optimization of ETLs in terms of passivation, post-fabrication treatment and choice of optimal materials [21-23], leaving research on HTL optimization vastly overlooked. In regular n-i-p architecture devices mostly two organic semiconductors have been used as HTL in the past: 2,2',7,7'-Tetrakis[N,N-di(4-methoxyphenyl)amino]-9,9'-spirobifluorene (spiro-OMeTAD) and Poly[bis(4-phenyl)(2,4,6-trimethylphenyl)amine] (PTAA) [24]. These compounds exhibit favorable solubility, reasonable energetic alignment with most perovskites and an amorphous nature. The main issues that arise from their usage involve poor conductivity and mechanical stability [25], the existence of pin-holes and a poor adhesion with the adjacent perovskite. There have been many studies trying to address these points and advance PSC performance through HTL optimization, but conventional approaches mainly focus on the doping strategies applied to these two materials [26-29].

Organic semiconductors spiro-OMeTAD and PTAA are traditionally doped with ionic p-dopant bis(trifluoromethane)sulfonimide lithium salt (LiTFSI) and 4-tertbutylpyridine (tBP). In the case of spiro-OMeTAD, in presence of oxygen, LiTFSI promotes its oxidation reaction by stabilizing its radical cation, resulting in the generation of mobile holes [30-32]. For PTAA, under illumination, a similar mechanism is proposed, whereby the oxidation of PTAA raises the conductivity of the polymer [33]. For both HTLs, the inclusion of tBP promotes a better distribution of the HTL on the perovskite, preventing organic semiconductor/LiTFSI phase segregation [34], thus leading to an improved morphology and uniformity of the resulting layer. However, its unfavorable long-term impact on stability indicates that new doping strategies might be required in the future [35,36]. For this, there have been efforts for finding cheap hydrophobic acidic substances with good solubility in solvents orthogonal to the underlying perovskite active layer. Such an alternative compound is tris(pentafluorophenyl)borane (BCF), which is an electrophilic Lewis acid that interacts with the organic semiconductor and increases its conductivity.

Here, we performed a dedicated study of the HTL/perovskite interface to evaluate the effects of dopants such as BCF on the interfacial potential landscape in working devices. In this work we chose four HTL doping configurations that have been reported for high-performing solar cells [24,37,38]: (i) spiro-OMeTAD doped with LiTFSI and tBP, (ii) spiro-OMeTAD doped with BCF (iii) PTAA doped with LiTFSI and tBP and (iv) PTAA doped with BCF. All the cells from all the batches were nominally identical, except for the HTL. We examined the potential distribution in all configurations via KPFM. We cleaved the devices and prepared smooth cross-sections by means of argon ion polishing. To get results that closely simulate the operation of working devices, we used a comprehensive static KPFM measurement protocol (See Supporting Information File 2) and measured potential profiles across all layers while

applying a voltage or under illumination. Our results indicate that the inclusion of BCF has a passivating effect on iodide defects within the devices. Particularly, a major improvement on the diode character of the HTL/perovskite interface was observed, in both spiro-OMeTAD and PTAA cells. The details of device fabrication, ion milling parameters and KPFM procedure are reported in the Experimental Section.

Results and Discussion

Efficiency Characterization

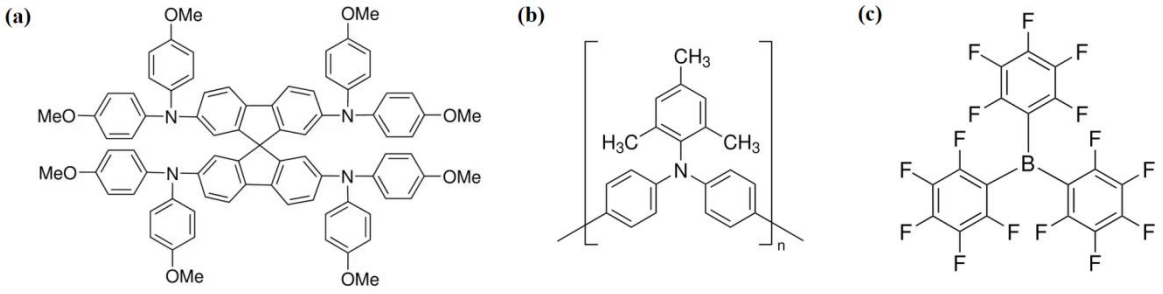

Figure 1: The structures of (i) spiro-OMeTAD, (ii) PTAA and (iii) BCF.

Whilst BCF has an advantageous impact on the conductivities of both spiro-OMeTAD and PTAA, when similar dopant concentrations are used, the effect on PTAA is more pronounced, which implies dissimilarities in the underlying doping mechanisms (See Supporting Information File 3). Nevertheless, we decided that for our BCF batches, the best approach was to dope both spiro-OMeTAD and PTAA solely with BCF and forgoing using further additives, in order to more directly evaluate the effect of BCF compared to the more traditional doping path of LiTFSI and tBP. The BCF concentration used in both cases was 8wt % with respect to the polymer repeating unit (PTAA), or molecular weight (spiro-OMeTAD).

To confirm the beneficial effect of the doping of the HTL with BCF, we initially characterized the photovoltaic performance of each of the four solar cell batches with a solar simulator under 1 Sun irradiation (1000 W/m^2). The corresponding parameters are reported in Table 1 and they refer to a statistical analysis of backwards scans from 10 devices of each batch. A slow scan rate of 60 mV/s was used for the current density-voltage (J-V) curves so as the ion distribution within the cell is under quasi-equilibrium [39].

Table 1: Solar cell device photovoltaic parameters employing different HTL doping strategies.

HTL doping strategy	J_{sc} (mA/cm^2)	V_{oc} (V)	FF (%)	PCE (%)
Batch 1: spiro-OMeTAD without BCF	22.3 ± 0.3	0.98 ± 0.15	74.1 ± 0.8	16.2 ± 0.3
Batch 2: spiro-OMeTAD with BCF	23.0 ± 0.8	1.04 ± 0.16	75.6 ± 2.6	17.3 ± 0.4
Batch 3: PTAA without BCF	23.3 ± 0.7	1.00 ± 0.14	75.4 ± 0.9	17.6 ± 0.4
Batch 4: PTAA with BCF	23.6 ± 0.6	1.01 ± 0.12	78.5 ± 0.2	18.7 ± 0.2

We notice that BCF had a beneficial effect on both spiro-OMeTAD and PTAA in terms of photovoltaic parameters. Whilst the positive effect on short-circuit current (J_{sc}) and open-circuit voltage (V_{oc}) is marginal, the increase on the fill factor (FF) is more

substantial, and is reflected on the elevated average power conversion efficiencies (PCE) of the batches. The average increased efficiency observed in the cells of batches that incorporated BCF can be attributed to the improved conductivity of the HTL material, as well as the passivation of mobile ionic defects. Specifically, these defects are prevented from drifting and accumulating at the interfaces of the perovskite and giving rise to non-radiative recombination sites, which diminish the HLT/perovskite junction quality [40,41]. To investigate the microscopic origins of these effects at the interfaces, we performed cross-sectional KPFM.

A well performing solar cell was selected from each batch and after cleaving, it was subjected to argon ion milling in order to get a smooth cross-section. This is useful for getting stable KPFM images, without electrostatic cross-talk. At every step of this procedure, the current-voltage characteristics were being monitored, as shown in Figure 2. By carefully selecting the parameters of the ion milling, we can ensure that the exposed interfacial structure is not damaged and the cells remain operational. Additionally, in order to interpret interfacial measurements more accurately, a precise characterization of the positions of the different solar cell layers is required. We identified the thickness and uniformity of the layers by comparing scanning electron microscopy (SEM) and atomic force microscopy (AFM) images (See Supporting Information File 4). The lateral resolution for both the AFM and SEM measurements is a few nanometers. The AFM channel that exhibited the clearest contrast between the layers was the amplitude error signal during the amplitude modulation topography scan. Figure S4 and Table S1 show the layered structure and layer thickness for each of the ion polished devices from the four batches. An important note that is highlighted by these measurements is that the optimal HTL thickness indicated by most spiro-OMeTAD PSC recipes is 200-370 nm, whereas that number for PTAA layers is much lower, around 40 nm [24]. The reduced bulk series resistance that comes with a thinner

layer is reflected in the superior J_{sc} values of PTAA cells. On the other hand, thinner HTLs pose a greater challenge in avoiding shunts, which makes device characterization via SEM essential.

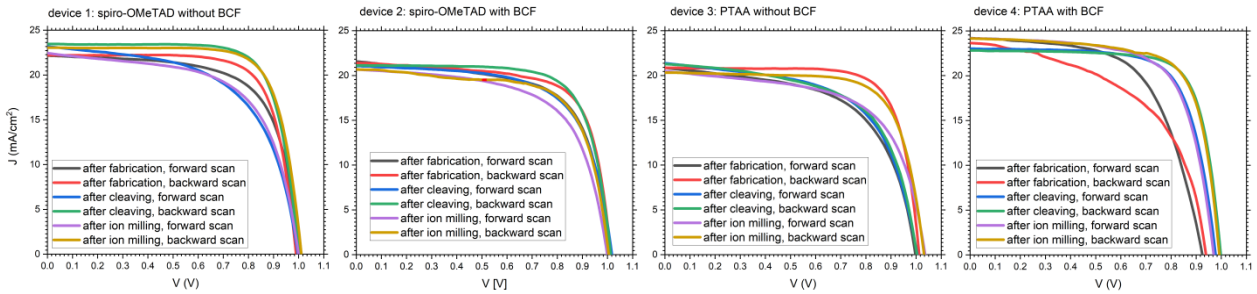

Figure 2: Current-voltage characteristics for the four solar cells that were chosen to be cleaved and polished for cross-sectional KPFM measurement. The plots show that the cells (that were ultimately measured with cross-sectional KPFM), survived both cleaving and consecutive ion milling without significant alteration to their performance. The paradoxically improved performance that is seen in some cleaved or ion milled cells can be attributed to either the well-documented self-healing of PSCs [42], or to difficulties accurately determining the active area of a cleaved solar cell.

To study the effect of different HTLs on the HTL/perovkite interfaces and how their choice affects charge extraction and recombination in our solar cells, we employed cross-sectional KPFM and specifically our measurement protocol for static KPFM, which allows us to evaluate the response of our cells under both applied voltages and under illumination.

KPFM characterization with an applied voltage

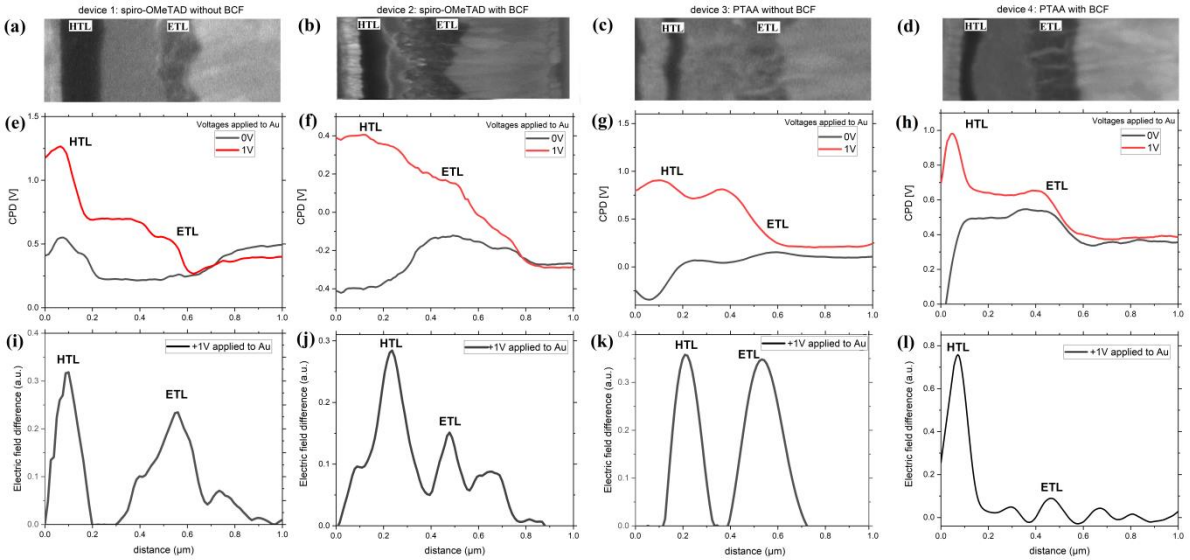

Figure 3: (a-d) SEM images showing the position of the hole and electron transport layers (HTL, ETL). (e-h) The CPD results of the cross-sectional KPFM measurement under dark/short circuit (black curves) and with an applied voltage of +1 V on the Au side (red curves, FTO side grounded). We apply +1 V because $V_{oc} \approx 1$ V. (i-l) The electric field difference built-up at the perovskite's interfaces, induced by the applied voltage.

When charges get generated, they drift to the sides of the device to externally recombine, or in the case of open-circuit, to accumulate, leading to forward biasing of the solar cell. Therefore, the surface potential profile of a forward biased device can be correlated with the potential distribution under illumination and open-circuit [43-45] (See Supporting Information File 2). By forward biasing, we bypass the open-circuit conditions and have a continuous charge flow within our devices, which operate with an external source of voltage. Consequently, charge transport can be studied, which depends on the diode characteristics of the interfaces. By biasing our devices with a

voltage value close to V_{oc}, we can plot the potential distribution across the layers of our solar cells and evaluate the charge extraction at their interfaces.

The CPD profile graphs under dark and short-circuit depend on the relative work function of the materials comprising the different layers of the devices. In Figure 3, the potential profiles plotted for the four devices exhibit features that deviate from the ideal profiles of a p-i-n junction (See Supporting Information File 1), with voltage drops and rises being apparent because of the band bending introduced by mobile ions or surface defect states caused by the cleaving. Furthermore, the CPD decrease on the HTL side relative to the perovskite when BCF is included in both cases reveals the p-doping of the HTL by the Lewis acid [46], whilst the increase of the perovskite CPD indicates an indirect n-doping induced by BCF. When subjecting the devices to a forward bias of 1V, which is approximately the value of the open-circuit voltage, we were able to observe potential profile distributions indicative of p-i-n junctions in all devices, with a lower CPD on the ETL side where the electrons accumulate under bias. Subtracting the first measurement from the second, we filter out all information from the data that does not pertain to potential changes due to charge separation and accumulation at the perovskite junctions because of the applied bias (like the aforementioned defect-state and relative work function contributions).

Consequently, we use these bias-induced potential profiles to plot electric field profiles [Figure 3(i-l)] that reflect the junction quality of the perovskite absorber with its adjacent transport layers.

To extract the electric field profiles we applied the equation:

$$\mathrm{E} = -\frac{\mathrm{dV}}{\mathrm{dx}}$$

Here, E is the electric field, V is the measured surface potential and x is the distance.

For these measurements, we applied +1 V to the Au electrode to forward bias the device [Figure 3(e-h)] (See Supporting Information File 5). The resulting magnitude of the electric field profile reflects the relative competition of the two junctions on either side of the perovskite to extract charges efficiently [47].

By applying a forward bias of approximately V_{oc}, we bring our cell into the same configuration as the open-circuit and illuminated case and we have a sufficient diffusive current flowing through the two junctions, but smaller in magnitude compared to current flowing through an ohmic contact. Therefore, the junction exhibiting the more rectifying behavior will still limit the current flow. For this model, the influence of the resistance of the active layer is omitted, as it remains the same for all devices tested. If the rectifying capability of the HTL/perovskite junction is poor, then under the applied bias, more ohmic-like current will readily flow through it and the voltage will mainly drop on the ETL interface, where the diode quality is better and less saturation current flows. This larger voltage drop corresponds to a larger electric field magnitude on the ETL side (Figure 4).

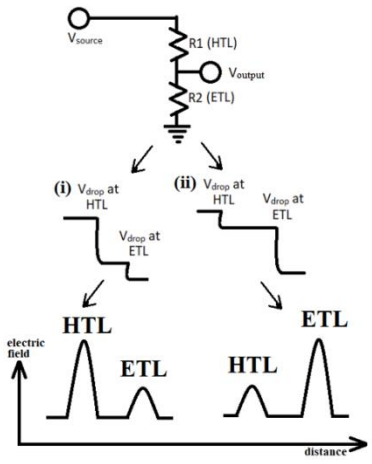

Figure 4: A schematic depicting a simple representation of the two perovskite junctions' interfacial resistances as resistors in a voltage divider. A resistor represents the ability of a diode junction to block current efficiently in reverse bias. (i) If R1>R2

(here: HTL shows better rectifying properties and a better diode quality than ETL), the voltage drops mostly at R1 (HTL). (ii) If R1<R2 (here: HTL exhibits a more ohmic behavior than ETL, because of a decreased charge extraction and more interfacial recombination), the voltage drops mostly at R2 (ETL). Given the identical ETLs of the four device batches we fabricated, we can directly compare the four different HTLs we used. The potential profiles are measured with cross-sectional KPFM and the electric field profiles are derived by the equation E=-dV/dx, since electrostatic fields are conservative.

In the case of the cells incorporating spiro-OMeTAD, from the J-V characterization, we expect the potential profiles of the cells with BCF to reflect the increased efficiency compared to the ones with LiTFSI/tBP. Indeed, from Figure 3(i,j) we can see that in both cases the HTL/perovskite junction exhibits a better diode quality relative to the ETL/perovskite interface. However, this effect is enhanced in the cell from the BCF batch. A better diode quality leads to a more efficient charge extraction/charge blocking on one interface relative to the other, so there is going to be a larger electric field difference due to the higher value of extracted charges at that interface. A similar circumstance arises in the PTAA solar cell when LiTFSI/tBP is replaced by BCF. Then, we notice a dramatic increase in the HTL field strength relative to the ETL, which reflects the improvement in the HTL/perovskite diode quality when BCF is incorporated [Figure 3(k,l)]. This result is associated with improved charge transport properties and a reduction in the number of trap states at that interface. We propose that BCF, as a Lewis acid electron acceptor, coordinates efficiently with under-coordinated iodide defects and passivates them, increasing junction quality, promoting p-doping and diminishing recombination at the HTL interface. This, in conjunction with the superior

PTTA/perovskite interaction and the favorable morphological properties of PTTA, leads to a considerable increase in the voltage drop at the hole extracting side of the device.

KPFM characterization under illumination and open-circuit

To study the quality of the HTL interfaces regarding recombination of photo-generated charge carriers, we illuminated the solar cell under open-circuit conditions and subtracted the dark/short-circuit profile, in order to extract the photo-carrier voltage. The resulting profile is independent from effects coupled to the built-in field, as well as from the aforementioned contributions of the relative work functions of the materials and possible surface defect states created from cleaving (See Supporting Information File 6). This time, the voltage is generated within the active area of the solar cell and the charge carriers are induced by the illumination. Unlike the previous experiment, where we considered charge transport as the reason for our results, we now force our devices to operate in open-circuit under a net zero charge flow condition. Therefore, charge recombination becomes the limiting factor that defines V_{oc} and device performance.

For devices 1 and 3 (without BCF), we can identify two diode junctions on either side of the perovskite absorber, that are almost equal in magnitude, whereas in devices 2 and 4 (with BCF) the HTL/perovskite junction clearly becomes the dominant one, as shown in Figure S8. Judging from the photo-charge built-up at the interfaces of the perovskite layer, for the solar cells that incorporate LiTFSI and tBP, there is not a single operation defining voltage drop, but rather both perovskite interfaces are approximately equal in their voltage drop magnitude and therefore contribute equally to charge extraction. Devices as such, that exhibit two charge separating junctions are more prone to charge recombination, compared to devices with just one junction [48]. On the contrary, devices that incorporate BCF-doped HTLs, exhibit one large drop at the

perovskite/HTL interface, indicative of the dominant diode junction that exists there. In order to further understand charge separation within the solar cells, we can use these photopotential profiles in order to examine charge extraction and accumulation within the solar cells.

By plotting charge density profiles we can more clearly point out the sum of photo-charge that has been extracted at the perovskite's interfaces and accumulated under open-circuit conditions. Unlike the measurements under bias, here we excite a large number of charges within the absorber, which diffuse, get extracted and aggregate at the interfaces, giving rise to a large charge density magnitude we can plot. In order to generate the photo-carrier density profiles, we applied Poisson's equation:

$$\rho_{photo}(x) = -\varepsilon_0 \varepsilon \frac{d^2}{dx^2} V_{photo}(x)$$

Here, ε_0 is the permittivity of free space, ε the relative permittivity of the perovskite material and V_{photo} the potential profile measured with KPFM.

Under open-circuit conditions, photo-generated free carriers are generated within the absorber material and diffuse to their corresponding side of the cell: electrons towards the ETL interface and holes towards the HTL interface. The relative ability of these interfaces to extract (and block) charges efficiently depends on the energetic alignment with the perovskite and the defect-induced interfacial recombination that occurs there. These factors determine the charge density that will ultimately accumulate on the cell's edges under open-circuit conditions.

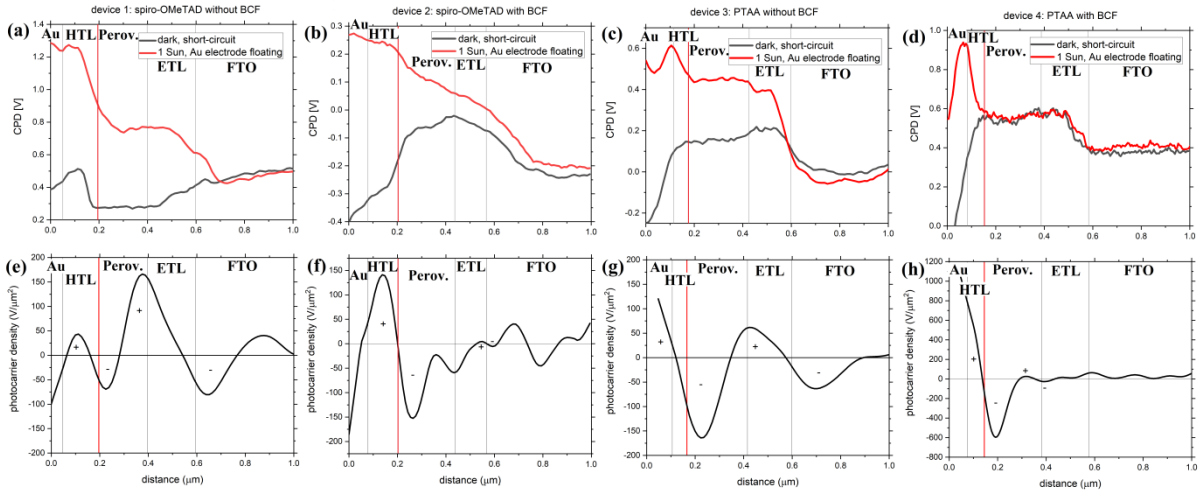

Figure 5: (a-d) The results of the cross-sectional KPFM measurement under illumination and open-circuit. The illumination was provided by a white-light source with irradiance similar to 1 Sun conditions. (e-h) Plots of the photo-charge density profiles ($\rho_{photo}(x)/\varepsilon_0\varepsilon$) across the device layers, with notations for positive and negative charge accumulation under open-circuit conditions.

In Figure 5(a-d) we can identify that in the case of the spiro-OMeTAD cell, there is an increase in the perovskite dark CPD, indicative of n-type doping, indirectly induced by the BCF additive. For the PTAA cell, the perovskite dark CPD also exhibited an increase relative to the CPD of the HTL. When illumination is turned on, the BCF-doped spiro-OMeTAD cell exhibits a linear CPD, indicative of a homogeneous electric field within the perovskite and a p-i-n junction, where charges can drift inside the perovskite to the corresponding interfaces. In the case of the PTAA cell, the CPD within the perovskite remained flat, indicating that the charge carriers have to diffuse to the interfaces and separate under the influence of the local fields there. In addition, when BCF was introduced in both spiro-OMeTAD and PTAA cells, the open-circuit photovoltage builds up more strongly at the HTL/perovskite interface, which indicates the increased charge separation potency of the junction because of decreased charge recombination rates.

In Figure 5(e-h) we again identify the charge separating junctions in each cell, as calibrated by the AFM and SEM images (Figure S4). In the cells that use spiro-OMeTAD as HTL, we can identify that positive charges get separated at the HTL/perovskite interface, whereas negative charges get separated within the mesoporous TiO_2. In the traditionally doped cell, we notice that on the HTL side there is a comparable amount of electrons and holes on each side of the junction. On the ETL side however, the positive charges on the perovskite side are more than the negative charges that have been extracted by the ETL, which leads to a positive charging of the perovskite. On the contrary, when BCF is added in the spiro-OMeTAD precursor solution, the HTL/perovskite interface extracts charges more efficiently and becomes the dominant junction relative to the one on the ETL side. A previous study [15] has associated the charging within the perovskite absorber under open-circuit conditions with unbalanced recombination rates of electrons and holes at its two interfaces. More specifically, a positive charging of the perovskite was connected with a preferential recombination of electrons at the HTL side. The elimination of this magnitude of positive built-up indicates that BCF has improved the junction quality in terms of charge carrier leakage and has diminished the defect-induced interfacial recombination by passivating iodide interstitials within the perovskite, which can transport to the interfaces and act as non-radiative recombination centers [49,50].

In the cells that use PTAA/BCF as HTL, we notice a large increase in the number of charges that get separated at the HTL junction compared to the ETL junction (in relation with the traditionally doped PTAA cell), which is indicative of the improvement in the junction quality on the HTL side that the BCF brings. Again, we propose that BCF is forming a Lewis adduct with under-coordinated halide ions that have migrated towards the HTL side and passivates them, diminishing interfacial recombination and increasing charge extraction [51,52]. In both cases of spiro-OMeTAD and PTAA cells,

the magnitude of charges at the HTL interface overtook the one at the ETL interface, which is proof of the increased HTL/perovskite junction quality and reduced recombination rates when BCF is included as additive.

Moreover, Hermes *et al*. [15] proposed the existence of an interlayer between HTL and perovskite, created by spiro-OMeTAD – iodide complex formation, which reduced efficiencies of solar cells. This was visible in cross-sectional KPFM results by way of a slight shift (≈70 nm) of the interfacial electron blocking layer into the spiro-OMeTAD. This interaction was said to de-dope spiro-OMeTAD and introduce a resistive layer that acted as a barrier for charge extraction. Such interaction between spiro-OMeTAD and iodide ions, as well as PTAA and iodide ions has also been reported elsewhere in the literature [53,54]. In Figure 5(e-h) (vertical red lines) we can see that both devices that do not include BCF exhibit this shift of the electron blocking interface (≈40 nm for the spiro-OMeTAD device, ≈45 nm for the PTAA device), which indicates the negative interaction of the mobile iodide defects that have diffused towards the hole extracting interface. On the contrary, the devices that incorporated BCF do not exhibit such shift, which suggests the successful passivation of iodide defects by the Lewis acid. We note that the spatial resolution of cross-sectional KPFM is sensitive enough to distinguish these slight shifts of tens of nanometers. This microscopically observed result translates to the macroscopic efficiency characterization, specifically the increased FF, which directly relates to a decrease in series resistance close to the HTL side of the device.

Conclusion

In conclusion, we incorporated BCF, an electrophilic substance with passivating properties, in the two most popular HTL semiconductors for PSCs. Current-voltage characterization indicated that the inclusion of BCF had a beneficial effect on the performance of both spiro-OMeTAD and PTAA cells. By applying our comprehensive static cross-sectional KPFM measurement protocol, we showed an increased junction quality and a reduced recombination rate for the HTL/perovskite interface of the selected characteristic devices from the batches that included BCF, compared to the ones from the batches that used the traditional doping method. Furthermore, for the devices that incorporated BCF, there is strong indication that the Lewis acid has a passivating effect on iodide defects, which accentuates the positive impact of BCF as an HTL additive for PSC performance enhancement. Cross-sectional KPFM provides a valuable tool for locally evaluating that impact and our set of measurements can act as a standard for evaluating devices for individual layer optimization.

Experimental

Solution and device preparation: For device fabrication, we mainly used the recipe of Klasen *et al*. [21]. We patterned fluorine-doped tin oxide (FTO) substrates on thin (1.1 mm) glass from Ossila (11 – 13 Ω/cm^2) with Zn powder and a 2 M HCl solution. Then, we brushed it thoroughly using a liquid alkanine concentrate (Hellmanex), followed by a 30 min argon plasma cleaning (200-G TePla Plasma System, Technics Plasma GmbH, at 0.14 mbar and 280 W). Consequently, we deposited a compact layer of TiO_2 via an aqueous 0.75 M $TiCl_4$ solution (Sigma-Aldrich, 99.99% trace metal basis). 80 µl of the solution was spin-coated at 5000 rpm for 30 s, and the resulting films were annealed at 500 ^oC for 30 min. Afterwards, we deposited a mesoporous TiO_2 layer

from a (transparent) titania paste solution (Aldrich, 16.67wt % in ethanol), via spin coating and annealed it (same parameters as previous step). After each of these titania deposition steps, we subjected the films to a UV-ozone cleaning step (FHR UVO 150) for 30 min, with an oxygen flow of 10 L/min. Then, a 1 M methylammonium lead iodide (MAPI) precursor solution was prepared (lead iodide 99.99% trace metals basis from TCI, methylammonium iodide >99.99% from Greatcell solar) with the materials dissolved in a DMF/DMSO (4:1) solvent and spin-coated using a two-step deposition (500 rpm for 10 s and 4000 rpm for 25 s). 150 µl of toluene were used as anti-solvent 10 s into the second step. The perovskite was crystalized during a 100 ^{o}C annealing step for 30 min. For the cells that incorporated spiro-OMeTAD, we used a solution containing 72.3 mg spiro-OMeTAD, 28.8 µl tBP and 17.5 µl LiTFSI solution (520 mg in 1 ml acetonitrile), all dissolved in 1 ml chlorobenzene (or BCF in chlorobenzene at an 8% mol ratio with spiro-OMeTAD, for the corresponding devices) and spin coated 80 µl at 4000 rpm for 30 s. For the cells that incorporated PTAA, we used a solution containing 15 mg PTAA, 7.5 µl, LiTFSI solution (170 mg in 1 ml acetonitrile) and 7.5 µl tBP solution (1:1 in acetonitrile), dissolved in 1 ml toluene. For the BCF batch, instead of LiTFSI and tBP, BCF was added in 8% mol ratio to PTAA. After the HTL deposition, an Au electrode was evaporated as a back contact, under vacuum (Edwards FL 400 Au evaporator). The devices were characterized in terms of efficiency with a solar simulator (Abet Technologies, SunLite) under AM1.5 illumination.

Cross-section preparation: To create solar cells with exposed cross-sections, we mechanically cleaved the solar cells along a direction perpendicular to their active layers, thus exposing their interfaces for direct measurement. In order to get a smooth cross-section we employed argon ion milling (Hitachi IM4000, discharge current: 130 µA, acceleration voltage: 2.5 kV, discharge voltage: 0.75 kV). Since argon is inert and

the process occurs under vacuum, we minimize the possibility for chemical contamination of our solar cells.

Kelvin probe force microscopy: Mapping the surface potential of the samples was conducted via an Asylum Research MFP3D microscope (Oxford Instruments) and an HF2LI-MOD lock-in amplifier (Zurich Instruments), in an argon atmosphere glove box (less than 1% ppm O_2 and negligible humidity). The cantilever used was SCM PIT V2 (resonance frequency: 75 kHz, spring constant: 3 N/m, Bruker). The scan rate of the measurement was 0.5 Hz. To increase the reliability of our data, we employed heterodyne-KPFM [55], whereby we mechanically excite the cantilever at its first resonant frequency, f_1, and electrically excite at a frequency of (f_2-f_1), where f_2 is the second resonant frequency [56]. Frequency mixing between the mechanical vibration at f_1 and the electrostatic force generates a sideband signal at frequency f_2, which is used as input for the KPFM feedback loop. For the extraction of the electric field and photocarrier density profiles from the surface potential data, we applied the definitional voltage equation for a conservative electric field and the Poisson equation, respectively. The profiles were smoothed with a 30 point adjacent-averaging method, to get smooth derivative curves with negligible noise.

Funding

This research was funded by the SPP2196 project (Deutsche Forschungsgemeinschaft).

References

1. Kojima, A., Teshima, K., Shirai, Y., Miyasaka, T. *Journal of the american chemical society* **2009**, 131(17), 6050-6051.

2. Green, M. A., Ho-Baillie, A., Snaith, H. J. *Nature photonics* **2014**, 8(7), 506-514.

3. Al-Ashouri, A., Köhnen, E., Li, B., Magomedov, A., Hempel, H., Caprioglio, P. Albrecht, S. *Science* **2020**, 370(6522), 1300-1309.

4. Yang, L., Feng, J., Liu, Z., Duan, Y., Zhan, S., Yang, S., Liu, S. *Advanced Materials* **2022**, 34(24), 2201681.

5. Stranks, S. D., Eperon, G. E., Grancini, G., Menelaou, C., Alcocer, M. J., Leijtens, T., Snaith, H. J. *Science* **2013**, 342(6156), 341-344.

6. Dong, Q., Fang, Y., Shao, Y., Mulligan, P., Qiu, J., Cao, L., Huang, J. *Science* **2015**, 347(6225), 967-970.

7. Shi, D., Adinolfi, V., Comin, R., Yuan, M., Alarousu, E., Buin, A., Bakr, O. M. *Science* **2015**, 347(6221), 519-522.

8. Johnston, M. B., Herz, L. M. *Accounts of chemical research* **2016**, 49(1), 146-154.

9. Chang, J., Xiao, J., Lin, Z., Zhu, H., Xu, Q. H., Zeng, K., Ouyang, J. *Journal of Materials Chemistry A* **2016**, 4(44), 17464-17472.

10. Garrett, J. L., Tennyson, E. M., Hu, M., Huang, J., Munday, J. N., Leite, M. S. *Nano letters* **2017**, 17(4), 2554-2560.

11. Yang, C., Du, P., Dai, Z., Li, H., Yang, X., Chen, Q. *ACS applied materials & interfaces* **2019**, 11(15), 14044-14050.

12. Noel, N. K., Habisreutinger, S. N., Pellaroque, A., Pulvirenti, F., Wenger, B., Zhang, F., Rand, B. P. *Energy & environmental science* **2019**, 12(10), 3063-3073.

13. Edri, E., Kirmayer, S., Mukhopadhyay, S., Gartsman, K., Hodes, G., Cahen, D. *Nature communications* **2014**, 5(1), 3461.

14. Bergmann, V. W., Weber, S. A., Javier Ramos, F., Nazeeruddin, M. K., Grätzel, M., Li, D., Berger, R. *Nature communications* **2014**, 5(1), 5001.

15. Hermes, I. M., Hou, Y., Bergmann, V. W., Brabec, C. J., Weber, S. A. *The journal of physical chemistry letters* **2018**, 9(21), 6249-6256.

16. Weber, S. A., Hermes, I. M., Turren-Cruz, S. H., Gort, C., Bergmann, V. W., Gilson, L., Berger, R. *Energy & Environmental Science* **2018**, 11(9), 2404-2413.

17. Hou, W., Ma, Y., Kang, J., Xiao, Y., Han, G. *Advanced Materials Interfaces* **2022**, 9(32), 2201259.

18. Li, Z., Xiao, C., Yang, Y., Harvey, S. P., Kim, D. H., Christians, J. A., Zhu, K. *Energy & Environmental Science* **2017**, 10(5), 1234-1242.

19. Tress, W., Marinova, N., Moehl, T., Zakeeruddin, S. M., Nazeeruddin, M. K., Grätzel, M. *Energy & Environmental Science* **2015**, 8(3), 995-1004.

20. Yu, H., Lu, H., Xie, F., Zhou, S., Zhao, N. *Advanced Functional Materials* **2016**, 26(9), 1411-1419.

21. Klasen, A., Baumli, P., Sheng, Q., Johannes, E., Bretschneider, S. A., Hermes, I. M., Berger, R. *The Journal of Physical Chemistry C* **2019**, 123(22), 13458-13466.

22. Kim, S., Zhang, F., Tong, J., Chen, X., Enkhbayar, E., Zhu, K., Kim, J. *Solar Energy* **2022**, 233, 353-362.

23. Li, F., Shen, Z., Weng, Y., Lou, Q., Chen, C., Shen, L., Li, G. *Advanced Functional Materials* **2020**, 30(45), 2004933.

24. Rombach, F. M., Haque, S. A., Macdonald, T. J. *Energy & Environmental Science* **2021**, 14(10), 5161-5190.

25. Le Corre, V. M., Stolterfoht, M., Perdigon Toro, L., Feuerstein, M., Wolff, C., Gil-Escrig, L., Koster, L. J. A. *ACS Applied Energy Materials* **2019**, 2(9), 6280-6287.

26. Cappel, U. B., Daeneke, T., Bach, U. *Nano letters* **2012**, 12(9), 4925-4931.

27. Burschka, J., Kessler, F., Nazeeruddin, M. K., Grätzel, M. *Chemistry of Materials* **2013**, 25(15), 2986-2990.

28. Nguyen, W. H., Bailie, C. D., Unger, E. L., McGehee, M. D. *Journal of the American Chemical Society* **2014**, 136(31), 10996-11001.

29. Watson, B. L., Rolston, N., Bush, K. A., Taleghani, L., Dauskardt, R. H. *Journal of Materials Chemistry A* **2017**, 5(36), 19267-19279.

30. Abate, A., Leijtens, T., Pathak, S., Teuscher, J., Avolio, R., Errico, M. E., Snaith, H. J. *Physical Chemistry Chemical Physics* **2013**, 15(7), 2572-2579.

31. Wang, S., Yuan, W., Meng, Y. S. *ACS applied materials & interfaces* **2015**, 7(44), 24791-24798.

32. Hawash, Z., Ono, L. K., Qi, Y. *Advanced Materials Interfaces* **2016**, 3(13), 1600117.

33. Kim, Y., Jung, E. H., Kim, G., Kim, D., Kim, B. J., Seo, J. *Advanced Energy Materials* **2018**, 8(29), 1801668.

34. Juarez-Perez, E. J., Leyden, M. R., Wang, S., Ono, L. K., Hawash, Z., Qi, Y. *Chemistry of Materials* **2016**, 28(16), 5702-5709.

35. Lamberti, F., Gatti, T., Cescon, E., Sorrentino, R., Rizzo, A., Menna, E., Franco, L. *Chem* **2019**, 5(7), 1806-1817.

36. Wang, S., Huang, Z., Wang, X., Li, Y., Günther, M., Valenzuela, S., Meng, Y. S. *Journal of the American Chemical Society* **2018**, 140(48), 16720-16730.

37. Luo, J., Xia, J., Yang, H., Chen, L., Wan, Z., Han, F., Jia, C. *Energy & Environmental Science* **2018**, 11(8), 2035-2045.

38. Liu, J., Liu, W., Aydin, E., Harrison, G. T., Isikgor, F. H., Yang, X., De Wolf, S. *ACS applied materials & interfaces* **2020**, 12(21), 23874-23884.

39. Courtier, N. E., Cave, J. M., Foster, J. M., Walker, A. B., Richardson, G. *Energy & Environmental Science* **2019**, 12(1), 396-409.

40. Ye, T., Wang, J., Chen, W., Yang, Y., He, D. *ACS Applied Materials & Interfaces* **2017**, 9(21), 17923-17931.

41. Ren, G., Han, W., Deng, Y., Wu, W., Li, Z., Guo, J., Guo, W. *Journal of Materials Chemistry A* **2021**, 9(8), 4589-4625.

42. Yu, Y., Zhang, F., Yu, H. *Solar Energy* **2020**, 209, 408-414.

43. Chen, Q., Mao, L., Li, Y., Kong, T., Wu, N., Ma, C., Chen, L. *Nature communications* **2015**, 6(1), 7745.

44. Lan, F., Jiang, M., Tao, Q., Li, G. *IEEE Journal of Photovoltaics* **2017**, 8(1), 125-131.

45. Lan, F., Jiang, M., Li, G. *IEEE 17th International Conference on Nanotechnology* **2017**, (pp. 379-382).

46. Marqués, P. S., Londi, G., Yurash, B., Nguyen, T. Q., Barlow, S., Marder, S. R., Beljonne, D. *Chemical Science* **2021**, 12(20), 7012-7022.

47. Xiao, C., Zhai, Y., Song, Z., Wang, K., Wang, C., Jiang, C. S., Al-Jassim, M. *ACS Applied Materials & Interfaces* **2023**, 15(17), 20909-20916.

48. Cai, M., Ishida, N., Li, X., Yang, X., Noda, T., Wu, Y., Han, L. *Joule* **2018**, 2(2), 296-306.

49. Zhang, X., Turiansky, M. E., Shen, J. X., Van de Walle, C. G. *Physical Review B* **2020**, 101(14), 140101.

50. Wiktor, J., Ambrosio, F., Pasquarello, A. *Journal of Materials Chemistry A* **2018**, 6(35), 16863-16867.

51. Yang, Z., Dou, J., Kou, S., Dang, J., Ji, Y., Yang, G., Wang, M. *Advanced Functional Materials* **2020**, 30(15), 1910710.

52. Wang, S., Wang, A., Deng, X., Xie, L., Xiao, A., Li, C., Hao, F. *Journal of Materials Chemistry A* **2020**, 8(25), 12201-12225.

53. Kim, H. S., Seo, J. Y., Park, N. G. *The Journal of Physical Chemistry C* **2016**, 120(49), 27840-27848.

54. Gueye, I., Shirai, Y., Khadka, D. B., Seo, O., Hiroi, S., Yanagida, M., Sakata, O. *ACS Applied Materials & Interfaces* **2021**, 13(42), 50481-50490.

55. Axt, A., Hermes, I. M., Bergmann, V. W., Tausendpfund, N., Weber, S. A. *Beilstein journal of nanotechnology* **2018**, 9(1), 1809-1819.

56. Garrett, J. L., Munday, J. N. *Nanotechnology* **2016**, 27(24), 245705.